Article

3D-CFD Modeling of Hollow-Fiber Membrane Contactor for CO$_2$ Absorption Using MEA Solution

Alexandru-Constantin Bozonc [ID], Vlad-Cristian Sandu, Calin-Cristian Cormos [ID] and Ana-Maria Cormos *

Faculty of Chemistry and Chemical Engineering, Babeș-Bolyai University, Arany Janos 11, 400028 Cluj-Napoca, Romania; alexandru.bozonc@stud.ubbcluj.ro (A.-C.B.); vlad.sandu@ubbcluj.ro (V.-C.S.); calin.cormos@ubbcluj.ro (C.-C.C.)
* Correspondence: ana.cormos@ubbcluj.ro

Abstract: Membrane technology is considered an innovative and promising approach due to its flexibility and low energy consumption. In this work, a comprehensive 3D-CFD model of the Hollow-Fiber Membrane Contactor (HFMC) system for CO$_2$ capture into aqueous MEA solution, considering a counter-current fluid flow, was developed and validated with experimental data. Two different flow arrangements were considered for the gas mixture and liquid solution inside the HFMC module. The simulation results showed that the CO$_2$ absorption efficiency was considerably higher when the gas mixture was channeled through the membranes and the liquid phase flowed externally between the membranes, across a wide range of gas and liquid flow rates. Sensitivity studies were performed in order to determine the optimal CO$_2$ capture process parameters under different operating conditions (flow rates/flow velocities and concentrations) and HFMC geometrical characteristics (e.g., porosity, diameter, and thickness of membranes). It was found that increasing the membrane radius, while maintaining a constant thickness, positively influenced the efficiency of CO$_2$ absorption due to the higher mass transfer area and residence time. Conversely, higher membrane thickness resulted in higher mass transfer resistance. The optimal membrane thickness was also investigated for various inner fiber diameters, resulting in a thickness of 0.2 mm as optimal for a fiber inner radius of 0.225 mm. Additionally, a significant improvement in CO$_2$ capture efficiency was observed when increasing membrane porosity to values below 0.2, at which point the increase dampened considerably. The best HFMC configuration involved a combination of low porosity, moderate thickness, and large fiber inner diameter, with gas flow occurring within the fiber membranes.

Keywords: CO$_2$ capture process; HFMC; absorption; 3D-CFD modeling

1. Introduction

Global warming has become a major issue in recent years due to the steady rise in greenhouse gas emissions. Carbon dioxide (CO$_2$) accounts for about 76% of total greenhouse gas emissions [1]. The rapid rate of growth of atmospheric CO$_2$ concentrations, from 280 ppm in 1850 to 418 ppm in 2022 [2], has driven a substantial increase in research concerning mitigation of CO$_2$ emissions. Carbon capture, utilization, and storage (CCUS) is a technology used to reduce CO$_2$ emissions and diminish the global warming phenomenon [3,4]. Among CCUS technologies, post-combustion technologies are the most convenient to implement on an industrial scale. The CO$_2$ separation process takes place after the combustion of fossil fuels in power plants or after the generation of products for other industrial processes (i.e., steel and iron production). As such, a complete overhaul of the existing industrial plant is not necessary and only the installation of an additional unit for CO$_2$ capture is required. There are various techniques applied in CO$_2$ capture, such as absorption, adsorption, and membrane-based and cryogenic separation [5–7]. Considering the advantages and disadvantages of these CO$_2$ capture methods, the post-combustion gas–liquid absorption process demonstrates enhanced viability due to its high absorption

capacity and low energy consumption [8,9], as well its ability to be integrated into existing power plants by introducing the CO_2 capture stage.

In the gas–liquid absorption process, the absorption solution represents a crucial component as the nature of the absorbent dictates the speed of absorption and also plays an important role in the dimensions of the absorber, with a faster reaction leading to a reduction in unit size. The most commonly used chemical solvents in the absorption of CO_2 are monoethanolamine (MEA), diethanolamine (DEA), methyldiethanolamine (MDEA), ammonia, and sodium hydroxide [2]. Among all alkanolamines, MEA is the most widely used in industrial processes, primarily due to its very fast reaction with CO_2 and high CO_2 absorption capacity. These properties enable the minimization of the absorption column dimensions and reduction of the liquid flow rate, inherently lowering the energy consumption associated with transportation, heating, and cooling. In addition, MEA has a low price and high water solubility. The disadvantages of MEA include high viscosity at high concentrations, high corrosion, and high regeneration energy [2,10].

Compared to conventional packed-bed columns, the use of hollow-fiber membrane contactors (HFMC) for CO_2 capture provides a considerable number of advantages, such as: (i) a significantly larger mass transfer area per unit volume, resulting in a smaller absorber; (ii) membrane systems are highly modular, so scale-up is simpler; (iii) the mass transfer area is constant and independent of hydrodynamic conditions; (iv) membrane systems are easier to replace or repair; (v) more environmental friendly; (vi) due to the physical separation between the two phases, the operating problems related to foaming, flooding, channeling, entrainment, and formation of emulsions are avoided; (vii) reduced loss of solvent; (viii) lower operating and investment costs; (ix) fluid flow rates are not limited to each other [10–14]. Given these advantages, the use of HFMC shows great potential for intensification of the gas–liquid absorption CO_2 capture process. However, there are also drawbacks to using HFMC for carbon capture, such as: (i) membranes introduce an additional mass transfer resistance for CO_2; (ii) transfer resistance increases significantly over time due to membrane watering; (iii) due to the short lifetime, the membranes need to be replaced periodically [2,10–12].

A schematic representation of the HFMC is presented in Figure 1, along with a representation of the CO_2 transfer from the gas phase into the liquid phase through the membrane pores.
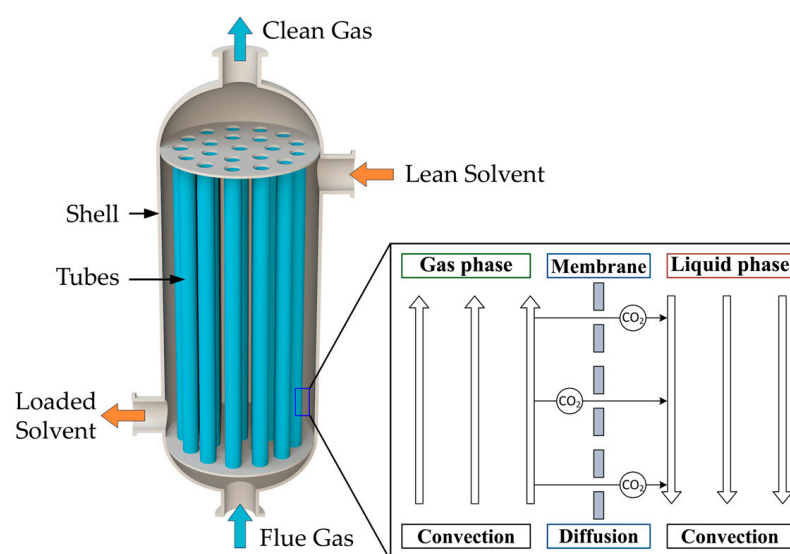

Figure 1. Schematic representation of the HFMC for CO_2 absorption.

The HFMC module consists of a large number of hollow cylindrical membranes inside the shell compartment. There are three distinct regions in the HFMC: the space inside the membranes—the tube side, the hollow-fiber porous membranes, and the space between the

membranes—the shell compartment. As the gas mixture flows inside the membrane tubes and the liquid absorbent solution flows between them in a counter-current arrangement, the membranes physically separate the two phases. The CO_2 diffuses from the gas phase through the membrane pores and is absorbed into the liquid solution, where it reacts with the MEA to form a stable compound. The resulting product will then be transported to the desorption column in order to obtain a high purity stream of CO_2 and regenerate the MEA solution (which is subsequently recycled to the absorption stage).

Several models for the capture of CO_2 using HFMC are presented in the literature, divided into one-dimensional (1D), two-dimensional (2D), and three-dimensional (3D) spatial models, based on the process-simplifying assumptions that have been made [15]. For the 1D models, the angular and axial variations of the process parameters are not accounted for, and only the variation over one dimension is considered. For these models, the radial direction is the one of interest, considering a series resistance for CO_2 mass transfer (i.e., resistance of gas, porous membrane, and liquid solution). Based on the two-film theory, the CO_2 will diffuse through the gas film, through the membrane pores and into the liquid solution. The mass transfer for each diffusion step can be represented with partial mass transfer coefficients, which can then be used to determine a global mass transfer coefficient [16]. In addition, the chemical reaction can also be integrated by using the enhancement factor brought by the reaction [17]. The 1D models available in the literature also consider different solvents for the absorption process and whether the membranes are wetted or not [18–23]. The 2D models suppose a single fiber inside the HFMC, considering the variation of parameters over the axial and radial directions occurring within the diffusive and convective transport mechanisms. The CFD modeling consists of a 2D axisymmetric spatial component, thus allowing the representation of a 3D geometry for one hollow-fiber membrane by revolving the 2D results around the axis of symmetry [24–32]. The 2D models provide a better understanding of the CO_2 absorption process using HFMC compared to the 1D models. However, the 2D models are limited to obtaining results for only a single fiber. The development of a 3D model is necessary to achieve higher accuracy and consider phenomena that are not captured in the 1D and 2D models, such as: non-uniform distribution of the fluids, non-uniform properties of the fluids and membranes, interaction between the fibers, etc. The main limitation of 2D models, compared to the 3D model developed in this work, is that they are axisymmetric and use the Happel's approximation model to determine the effective radius of the shell around one membrane. Additionally, the 3D model also considers the fluid distribution around the shell wall, an effect that is also overlooked in the available 2D models. A drawback to the increased complexity enabled by the 3D models is the requirement to use more computational resources in order to solve the governing equations. There is a limited number of 3D models currently available in the literature [33–35], indicating substantial potential for the development of 3D models for membrane-based CO_2 capture [15].

In this work, a comprehensive computational fluid dynamics (CFD) 3D model of the HFMC system for CO_2 capture considering an aqueous MEA solution and counter-current fluid flow is developed and validated with experimental data. The novelty of this work lies in the modeling and simulation of the full 3D HFMC geometry for CO_2 capture. The effect of different operating conditions (flow rates/flow velocities and concentrations) and HFMC geometrical characteristics (porosity, number, inner diameter, thickness, and length of fiber membranes) on CO_2 capture process parameters is investigated. In addition, the impact of how the fluids flow inside the fiber membrane module is evaluated.

2. Mathematical Model Approach

The CFD model for CO_2 absorption was developed using COMSOL Multiphysics, implementing the HFMC geometry represented in Figure 2. In Figure 2a, the entire HFMC geometry is represented, containing 510 membranes arranged symmetrically under a hexagonal distribution inside the shell. In order to reduce the simulation time and the computational resources needed, the complete HFMC module is sliced into four symmet-

rical parts (Figure 2b), resulting in only a quarter of the HFMC module being simulated. A 2D horizontal section of the simulated geometry is represented in Figure 2c, where the hexagonal symmetrical distribution can be better observed, as well as the distinct sections of the geometry (i.e., tubes—inside the membranes, membranes, and the shell compartment). A section through one of the membranes is represented in Figure 2d. The gas mixture flows inside the membranes (i.e., tubes) and the liquid MEA solution flows between the membranes (i.e., shell) in a counter-current arrangement.
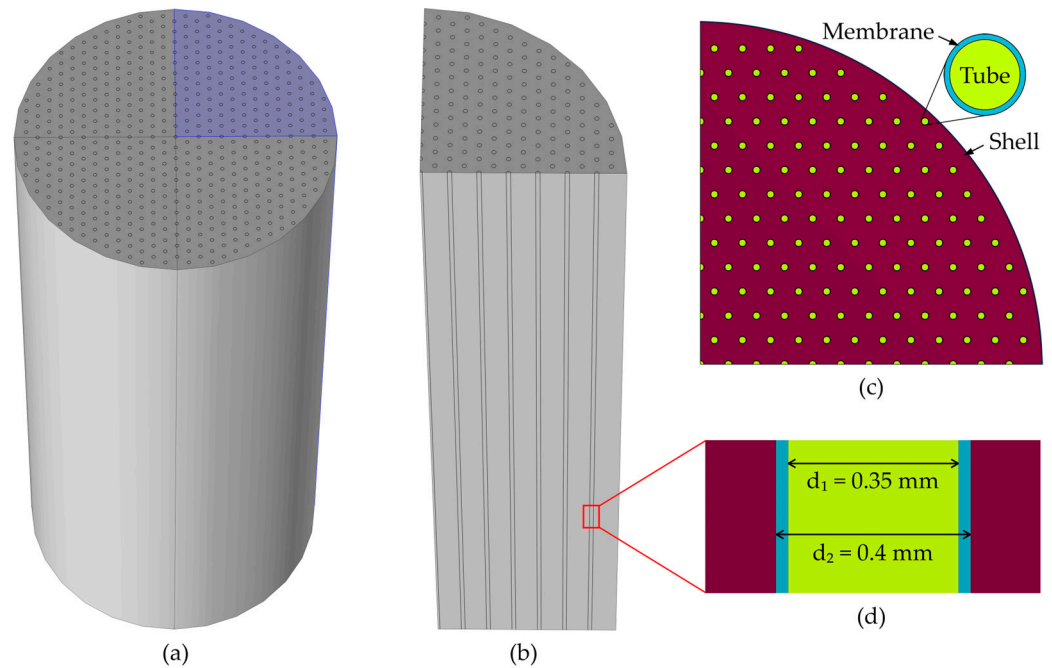

Figure 2. (**a**) 3D HFMC geometry representation, (**b**) quarter of the HFMC 3D representation, (**c**) 2D horizontal section representation of the distribution of membranes in the shell of the HFMC, (**d**) 2D vertical section representation of a membrane.

The mesh used to spatially discretize the HFMC in the CFD model is represented in Figure 3.
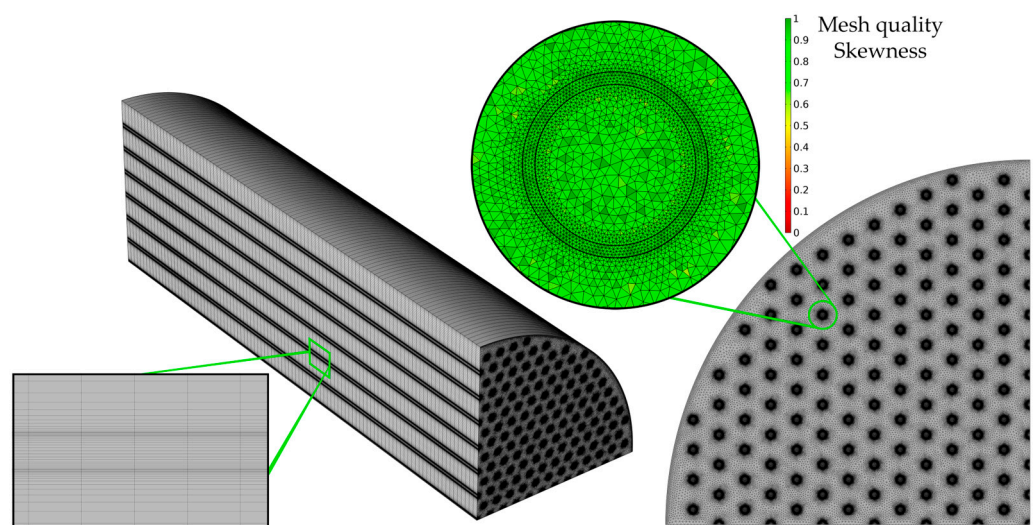

Figure 3. Mesh of the HFMC and quality of the mesh.

The geometry was sliced in 100 equal pieces. The mesh for each slice (presented in the right corner of Figure 3) consists of a triangular mesh, with an increase in element density in the regions of interest: inside and around the membranes, as this is where CO_2 from the gas phase diffuses through the membrane, is absorbed in the liquid, and reacts with the MEA. In addition, the mesh quality is presented in terms of element skewness, with green representing the highest quality. The mesh was sufficiently refined until mesh convergence was reached and the model predicted mesh-independent results. The number of mesh elements for a single fiber membrane was 130,800 (the elements for all membranes in the implemented geometry was 16,731,100), 166,000 for discretization of a tube (all tubes required 20,979,300 elements), and 34,107,600 for the shell, with a total average quality of about 0.85.

The HFMC characteristics are presented in Table 1, along with the process operating conditions, which are represented in Table 2.

Table 1. HFMC Polypropylene (PP) module characteristics [31].

Parameters	Value	Unit
Membrane inner radius (r_1)	0.175	mm
Membrane outer radius (r_2)	0.2	mm
Number of membranes (n)	510	-
Module inner radius (r_{mod})	1.75	cm
Membrane length (L)	27	cm
Membrane porosity (ε_{mem})	0.17	-
Membrane tortuosity (τ_{mem})	19.7	-
Average pores radius (r_p)	0.05	μm

Table 2. Process operating conditions [31].

Parameters	Value	Unit
Gas flow rate (Q_G)	1–3	L/min
Liquid flow rate (Q_L)	10–30	L/h
CO_2 gas concentration (C_{CO_2})	10	vol%
MEA liquid concentration (C_{MEA})	5	wt%
Temperature (T)	298	K
Pressure (P)	1	bar

In order to develop the CFD model for CO_2 absorption using HFMC, the following assumptions have been made:

- Isothermal conditions for the fluids;
- The membranes are operating in non-wet condition;
- The CO_2 solubility in aqueous MEA solution is calculated with Henry's law;
- Fully developed laminar flow for both fluid phases (i.e., gas and liquid).

The 3D CFD model of the HFMC was implemented in COMSOL Multiphysics 6.1, using a 64-bit operating system, with two Intel(R) Xeon(R) Platinum 8168 CPU @ 2.70 GHz and 512 GB of RAM.

2.1. Continuity Equation

The equations are solved in dynamic conditions, therefore the continuity equations (i.e., conservation of mass) for both phases are:

$$\frac{\partial}{\partial t}(\rho_i) + \nabla \cdot (\rho_i u_i) = 0 \tag{1}$$

2.2. Navier–Stokes Equations—Tubes and Shell

The flow regimes for the gas mixture inside the tubes and the liquid solution inside the shell are determined by calculating the Reynolds numbers with values of 18.4 and 44, respectively, indicating laminar flow types for both phases. In order to solve the laminar flows inside the membranes and surrounding them, the model used the continuity equations (Equation (1)) and the Navier–Stokes equations (i.e., conservation of momentum) (Equation (2)):

$$\rho_i \frac{\partial u_i}{\partial t} + \rho_i (u_i \cdot \nabla) u_i = \nabla \cdot (-p_i I + \tau_i) \tag{2}$$

where τ_i is the viscous stress tensor, calculated using (Equation (3)):

$$\tau_i = \mu_i \left(\nabla u_i + (\nabla u_i)^T \right) - \frac{2}{3} \mu_i (\nabla \cdot u_i) I \tag{3}$$

2.3. Species Transport—Tubes

In the gas phase, there is no chemical reaction, therefore the mass transfer of species inside the membranes is described only by convection and diffusion, considering an isotropic diffusion (Equation (4)):

$$\frac{\partial c_j}{\partial t} + \nabla \cdot \left(-D_{j,G} \nabla c_j \right) + u \cdot \nabla c_j = 0 \tag{4}$$

Equation (5), known as the Graetz–Lévêque solution [10], is used to predict the partial mass transfer coefficient of CO_2 inside the membranes (i.e., tube side):

$$Sh_{tube} = \frac{k_{CO_2,g} d_1}{D_{CO_2,g}} = 1.62 \left(\frac{d_1}{L} Re \right)^{0.33} \tag{5}$$

2.4. Species Transport—Membranes

The mass transfer in the hydrophobic microporous membranes is represented by the convection and diffusion of gas components through the membrane pores, which are considered to be filled only with gas as the membrane functions in a non-wet state (Equation (6)):

$$\varepsilon_{mem} \frac{\partial c_j}{\partial t} + \nabla \cdot \left(-D_{j,mem} \nabla c_j \right) + u \cdot \nabla c_j = 0 \tag{6}$$

The effective diffusion coefficient of component j through the membrane pores $D_{j,mem}$ is calculated considering the membrane porosity ε_{mem} and tortuosity τ_{mem} (Equation (7)), assuming an isotropic diffusion:

$$D_{j,mem} = \frac{\varepsilon_{mem}}{\tau_{mem}} D_{j,G} \tag{7}$$

The partial mass transfer coefficient of CO_2 through the membrane is determined using Equation (8) [26]:

$$k_{CO_2,mem} = \frac{D_{CO_2,mem}}{\delta_{mem}} \tag{8}$$

2.5. Species Transport—Shell

Inside the shell compartment, the CO_2 absorbed from the gas phase into the liquid solution reacts with MEA. Therefore, the equation that describes mass transfer inside the shell (Equation (9)) also contains the chemical reaction rate R_j, together with terms for diffusion and convection:

$$\frac{\partial c_j}{\partial t} + \nabla \cdot \left(-D_{j,L} \nabla c_j \right) + u \cdot \nabla c_j = R_j \tag{9}$$

According to Yang and Cussler in their work on gas absorption and stripping, the partial mass transfer coefficient of CO_2 inside the shell side, where fluid flow is parallel to the fibers, can be calculated with Equation (10) ($0.5 < Re < 500$) [36]:

$$Sh_{shell} = \frac{k_{CO_2,l}d_h}{D_{CO_2,l}} = 1.25 \left(Re \frac{d_h}{L} \right)^{0.93} Sc^{0.33} \tag{10}$$

According to the double-film theory, the overall resistance of mass transfer is the sum of the resistances of all layers through which the CO_2 diffuses. The resistance of each layer can be measured by calculating the inverse of the partial mass transfer coefficient of CO_2, indicating the difficulty for the CO_2 molecules to diffuse through that particular layer (fluid or material). Therefore, the overall mass transfer coefficient of CO_2 based on the liquid phase can be calculated using the sum of the three mass transfer resistances inside of the HFMC: liquid ($1/k_{CO_2,l}$), membrane ($1/k_{CO_2,m}$), and gas ($1/k_{CO_2,g}$), while also accounting for the dimensions of the system and the CO_2 solubility in the absorbent solution, as shown in Equation (11) [37]:

$$\frac{1}{K_L d_2} = \frac{1}{k_{CO_2,l}d_2} + \frac{1}{k_{CO_2,m}H_{CO_2}d_{lm}} + \frac{1}{k_{CO_2,g}H_{CO_2}d_1} \tag{11}$$

The CO_2 mass transfer flux from the gas phase to the liquid phase is calculated based on the overall mass transfer coefficient of CO_2, the concentration gradient at the gas–liquid interface, and the absorption enhancement factor E given by the chemical reaction (Equation (12)) [23]:

$$J_{CO_2} = E \cdot K_L \cdot \left(\frac{C_{CO_2}^g}{H_{CO_2}} - C_{CO_2}^L \right) \tag{12}$$

The reaction of CO_2 and MEA, which takes place within the liquid phase located in the shell compartment of the HFMC, is described by the following reaction rate expression [26]:

$$R_{CO_2-MEA} = \frac{10^{(10.99-2152/T_L)}}{1000} C_{CO_2}^L C_{MEA}^L \tag{13}$$

The efficiency of the absorption process of CO_2 using HFMC in an MEA solution is calculated using Equation (14), considering the variation in CO_2 concentration in the flue gas and the clean gas:

$$CO_2 \text{ capture rate} = \left(1 - \frac{C_{CO_2,outlet}}{C_{CO_2,inlet}} \right) \cdot 100 \tag{14}$$

3. Results and Discussion

The CFD model for the CO_2 absorption process in an MEA solution using HFMC was implemented with the membrane module characteristics presented in Table 1 at different operating conditions (Table 2).

3.1. Model Validation

The CFD model of the HFMC for CO_2 absorption was validated with experimental data published in the literature [31]. The validation was performed by comparing the experimental data with the simulation results in terms of CO_2 capture rate (Equation (14)), at various liquid flow rates (Figure 4), gas flow rates (Figure 5), and CO_2 gas inflow concentrations (Figure 6). Overall, the simulation results showed excellent agreement with the experimental data, with $R^2 > 0.922$, demonstrating that the developed CFD model represented the process of CO_2 absorption in an MEA solution using HFMC with high accuracy.
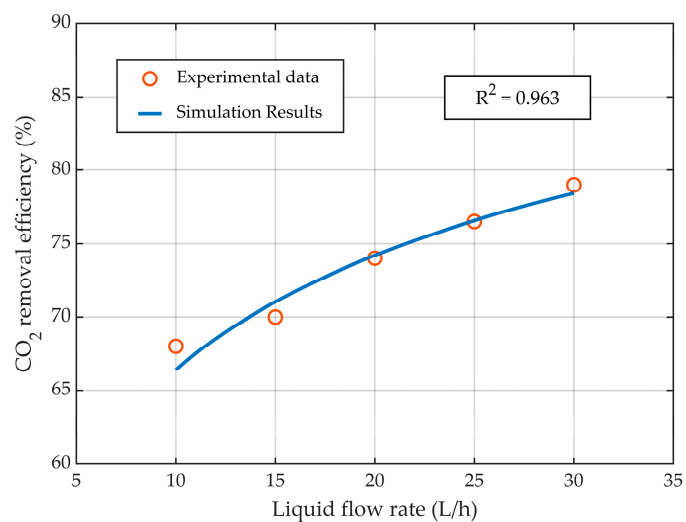
Figure 4. CO_2 capture rate profile at different liquid flow rates, at a constant gas flow rate of 2 L/min.
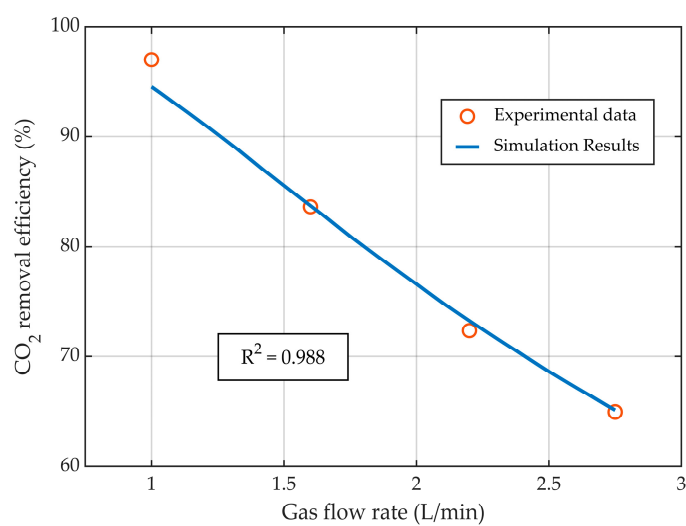

Figure 5. CO_2 capture rate profile at different gas flow rates, at a constant liquid flow rate of 25 L/h.
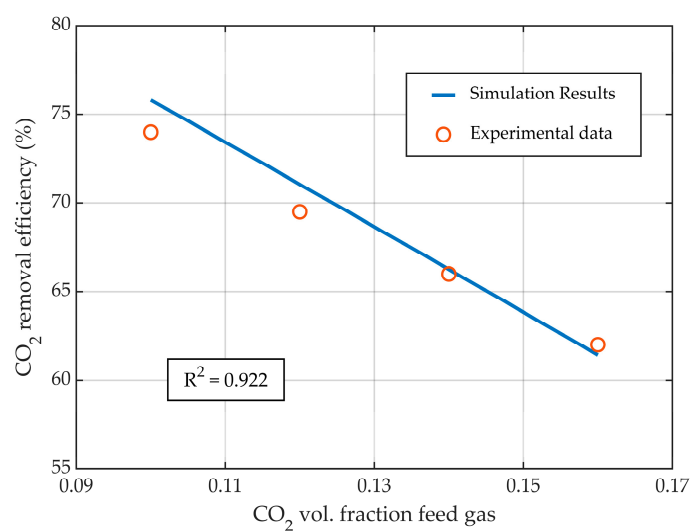

Figure 6. CO_2 capture rate profile at different inflow CO_2 concentration in gas phase, at constant gas (2 L/min) and liquid flow rates (25 L/h).

By increasing the liquid flow rate and maintaining a constant gas flow rate, the absorption efficiency of CO_2 showed an increase (Figure 4) due to the rise in the amount of MEA that flowed inside the HFMC and reacted with the absorbed CO_2. Comparing the experimental data with the simulation results, a very good correlation was observed, with an $R^2 = 0.963$. The CO_2 removal efficiency was increased from about 66.5% to nearly 79% for values of the liquid flow rate ranging from 10 L/h to 30 L/h, respectively.

While maintaining the liquid flow rate constant at 25 L/h, the increase in the gas flow rate determined a decrease in CO_2 capture rate (Figure 5) due to the reduction in the CO_2 residence time inside the HFMC. The experimental data and the simulation results exhibited a very good correlation, with an R^2 value of nearly 0.99. By increasing the gas flow rate from 1 L/min to 2.75 L/min, the CO_2 absorption efficiency decreased from 94.5% to nearly 65%, respectively.

The increase in the concentration of CO_2 in the inflow gas led to a decrease in the absorption efficiency of CO_2 (Figure 6), while maintaining constant gas and liquid flow rates, due to the increase in the amount of CO_2 in the gas phase. The simulation results were in good agreement with the experimental data, with an $R^2 = 0.922$. Changing the CO_2 concentration in the inflow gas from 0.1 to 0.16 vol. fraction, the CO_2 removal efficiency was decreased from nearly 76% to 61.5%, respectively.

3.2. Velocity Profiles

The gas velocity inside the membranes, within the tubes, is represented in Figure 7a. The velocity profile predicted by the model showed a typical laminar shape for fluid flow inside a tube.
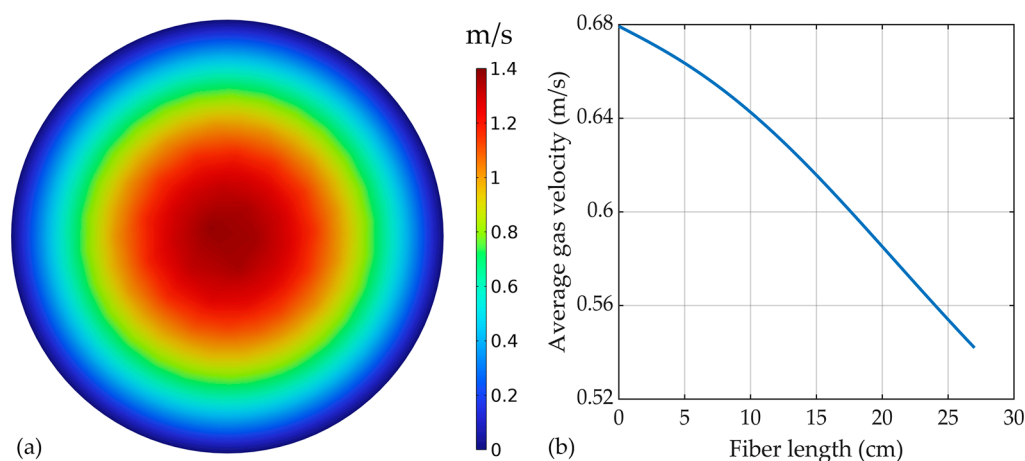

Figure 7. (**a**) Gas mixture velocity profile inside the tubes, (**b**) average gas velocity profile along the HFMC length. Gas flow rate of 2 L/min.

The maximum velocity was observed in the center of the tubes, at around 1.37 m/s (*Re* = 14), while a decreasing velocity was seen closer to the inside membrane wall, with values of zero at the contact with the membrane, due to the friction with the membrane wall and the no-slip boundary conditions assumed at the wall. The average gas velocity profile along the HFMC module is presented in Figure 7b. A reduction in the gas velocity from around 0.68 m/s at the inlet to 0.542 m/s at the outlet of the HFMC module.

The solution for the liquid phase velocity profile surrounding the membrane tubes is represented in Figure 8, with the maximum velocity of the liquid seen between the membranes, at around 0.0132 m/s (*Re* = 37). The liquid velocity was decreasing closer to the membranes and module walls, with a velocity near zero where the friction between the fluid and the walls was highest at the edges.
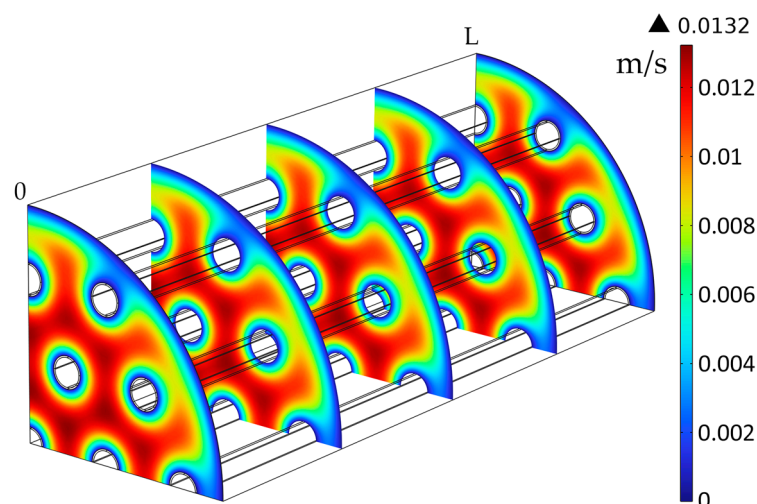
Figure 8. Liquid velocity profile in the shell compartment, Q_L = 25 L/h.

3.3. Concentration Profiles

The CO_2 concentration in the gas phase inside the membranes (tubes) decreased over the length of the membranes, from about 4.06 mol/m^3 at the tube inlet to nearly 0.62 mol/m^3 at the outlet, resulting in a CO_2 absorption efficiency of about 84.7% due to the absorption in the liquid phase (Figure 9). The concentration was maximum in the middle of the tubes and was decreasing in the radial direction of the tubes and along the membrane thickness due to diffusion.
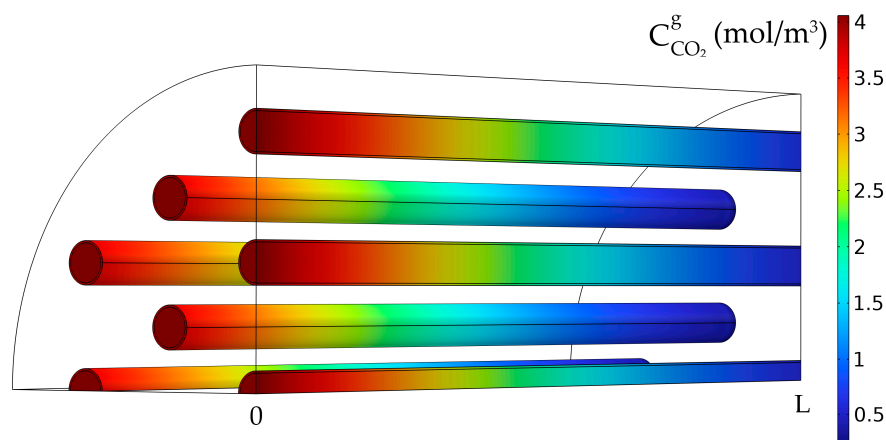

Figure 9. CO_2 gas concentration in the tubes. $C_{MEA,0}$ = 818 mol/m^3 (5 wt%), $C_{CO_2,0}$ = 4.06 mol/m^3 (10 vol%), Q_g = 2 L/min, Q_L = 25 L/h.

For the absorbent solution, which flows between the membranes in the shell, the MEA concentration was also decreasing along the membrane length and around the membranes due to the reaction with the absorbed CO_2 (Figure 10). The MEA concentration decreased along the length of the membranes from 818 mol/m^3 at the inlet to about 720 mol/m^3 at the exit of the HFMC. The concentration decreased around the membranes and was lower closer to the membrane walls due to the reaction with the absorbed CO_2 from the gas phase, while a higher concentration was seen further in the liquid phase, far from the membranes. The absorbed CO_2 reacted first with the MEA close to the membrane walls, then the CO_2 diffused inside the liquid phase further into the liquid solution, which resulted in the concentration gradient around the membranes.
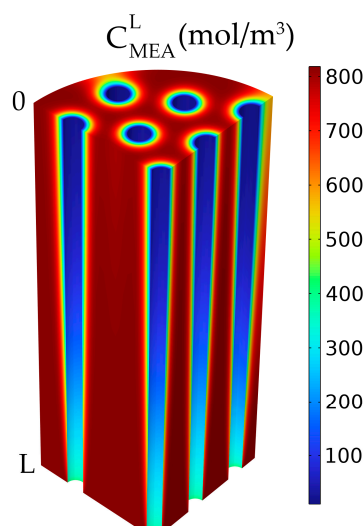
Figure 10. MEA liquid concentration in the shell compartment. $C_{MEA,0}$ = 818 mol/m^3 (5 wt%), $C_{CO_2,0}$ = 4.06 mol/m^3 (10 vol%), Q_g = 2 L/min, Q_L = 25 L/h.

3.4. Tubes vs. Shell

Two different ways for the flow of the gas mixture and liquid solution were considered inside the HFMC module.

In the first case, the gas mixture flowed inside the membranes and the liquid MEA solution between them (Figure 11a), while in the second case, the liquid flow was considered inside the membrane and the gas between them (Figure 11b). In both cases, counter-current flow was assumed, with constant flow rates and compositions.
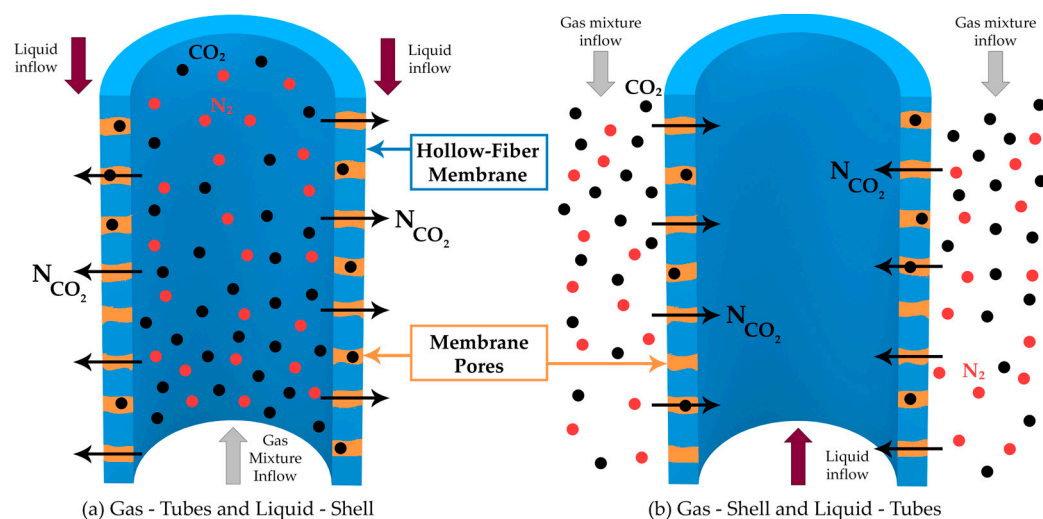

(a) Gas - Tubes and Liquid - Shell   (b) Gas - Shell and Liquid - Tubes

Figure 11. (**a**) Gas mixture inside the membranes (Tubes) and Liquid solution between membranes (Shell), (**b**) Gas mixture between membranes (Shell) and Liquid solution inside the membranes (Tubes).

Regardless of flow configuration (Figure 11), increasing the gas flow rate showed a decrease in the absorption rate of CO$_2$ (Figure 12) due to the decrease in the overall residence time for the gas phase. When the gas mixture flowed inside the membranes and the liquid aqueous MEA solution between them (Figure 11a), the absorption efficiency decreased from about 94.5% at a gas flow rate of 1 L/min to 62.8% at a gas flow rate of 3 L/min. In the other case, when the gas mixture passed between the membranes and the liquid absorption solution ran inside them (Figure 11b), the CO$_2$ capture rate decreased from 81% at a gas flow rate of 1 L/min to 43.3% at a gas flow rate of 3 L/min. Over the entire range of gas flow variation, the absorption efficiency was considerably higher

for the case when the gas mixture flow inside the membranes and the liquid solution between them (Figure 11a). At a gas flow rate of 1 L/min, the difference in absorption efficiency between the two configurations was 13.5%, while at a gas flow rate of 3 L/min, the difference increased to 19.5%.
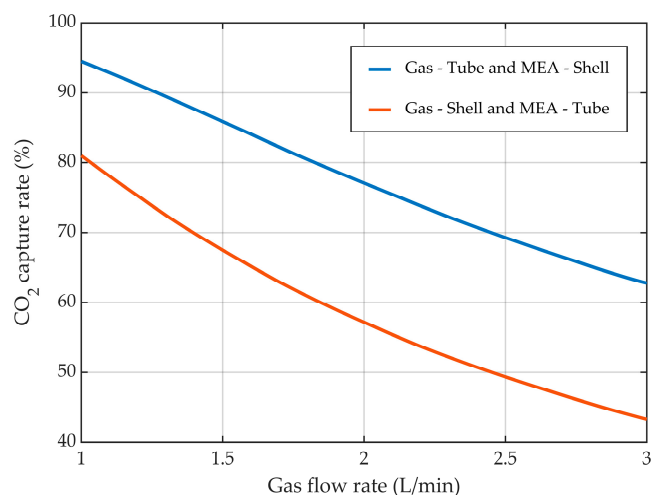

Figure 12. CO_2 capture rate at different gas flow rates. $C_{MEA,0}$ = 818 mol/m^3 (5 wt%), $C_{CO_2,0}$ = 4.06 mol/m^3 (10 vol%), Q_L = 25 L/h.

The effect of the liquid flow rate considering the two different flow configurations inside the HFMC is represented in Figure 13. The increase in the liquid flow rate resulted in an increase in the CO_2 capture rate. When the gas mixture flowed inside the membranes and the liquid aqueous MEA solution between them, the absorption efficiency increased from about 66.5% at a liquid flow rate of 10 L/h to nearly 78.5% at a liquid flow rate of 30 L/h. In the other case, when the gas mixture passed between the membranes and the liquid absorption solution inside them, the CO_2 capture rate increased from 46.5% at a liquid flow rate of 10 L/h to 58.8% at a liquid flow rate of 30 L/h. Along the entire range of investigated liquid flow rates, the absorption efficiency was considerably higher in the case when the gas mixture ran inside the membranes and the liquid solution between them, with a near constant difference between the two cases of around 12.2%.
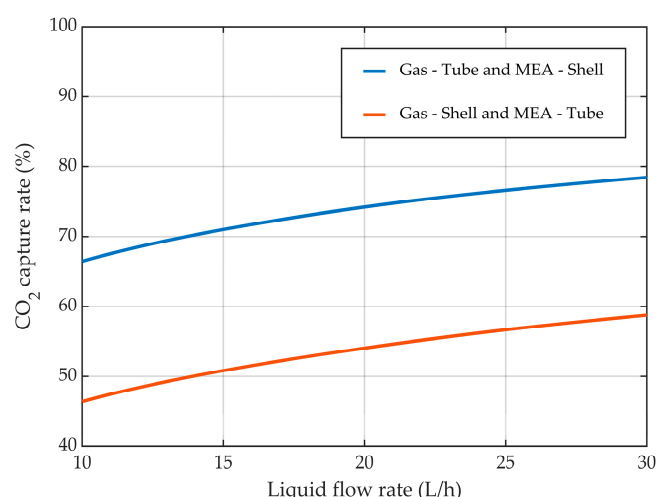

Figure 13. CO_2 capture rate at different liquid flow rates. $C_{MEA,0}$ = 818 mol/m^3 (5 wt%), $C_{CO_2,0}$ = 4.06 mol/m^3 (10 vol%), Q_g = 2 L/min.

3.5. Membrane Dimensions

An important factor in the absorption process of CO_2 using HFMC is the dimensions of the membranes, as the mass transfer area between gas and liquid is primarily dictated

by the radius of the membrane and the mass transfer resistance through the pores is determined by the thickness of the membrane.

3.5.1. Constant Membrane Thickness

The CO_2 mass transfer resistance through the membrane pores was kept consistent by maintaining a constant membrane thickness. By increasing the membrane radius, the mass transfer area between the gas mixture and liquid solution increased and the gas velocity decreased, resulting in a higher residence time for the gas phase and an increase in the CO_2 removal efficiency (Figure 14), from around 58.5% for the membrane inner radius of 0.1 mm to nearly 99.5% for a membrane radius of 0.5 mm.
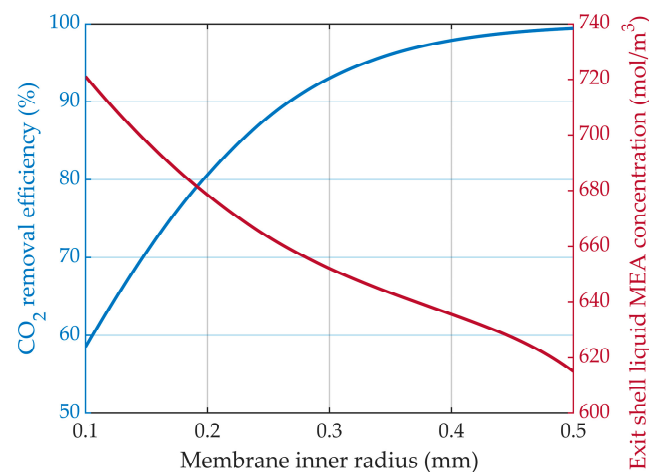

Figure 14. CO_2 removal efficiency and liquid MEA shell exit concentration profiles at different membrane inner radii and a constant membranes thickness of 0.025 mm. $C_{MEA,0}$ = 818 mol/m^3 (5 wt%), $C_{CO_2,0}$ = 4.06 mol/m^3 (10 vol%), Q_g = 2 L/min, Q_L = 25 L/h.

The liquid MEA concentration decreased from about 720 mol/m^3 for a membrane inner radius of 0.1 mm to 615 mol/m^3 for a membrane inner radius of 0.5 mm.

The MEA concentration decreased along the membrane length and around them due to the reaction with the absorbed CO_2. The liquid MEA concentration 3D profiles in the liquid phase surrounding the membranes, for different membrane inner radius values but constant thickness, are represented in Figure 15. The increase in the membrane radius led to an increase in the liquid velocity inside the shell compartment of the HFMC.
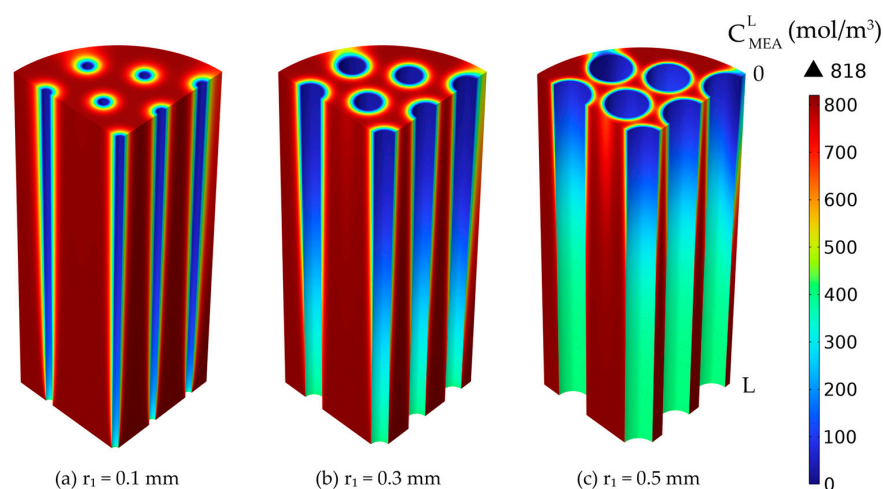

(a) r_1 = 0.1 mm   (b) r_1 = 0.3 mm   (c) r_1 = 0.5 mm

Figure 15. Liquid MEA concentration profiles in the shell compartment, constant membrane thickness 0.025 mm and variable inner radius: (**a**) 0.1 mm, (**b**) 0.3 mm, (**c**) 0.5 mm. $C_{MEA,0}$ = 818 mol/m^3 (5 wt%), $C_{CO_2,0}$ = 4.06 mol/m^3 (10 vol%), Q_g = 2 L/min, Q_L = 25 L/h.

3.5.2. Variable Membrane Thickness—r_2 Constant

By increasing the membrane thickness, the inner radius decreased, meaning that the velocity for the fluid that ran in the tubes (i.e., the gas mixture) increased, leading to a decrease in the overall residence time of CO_2 inside the HFMC. In addition, increasing the membrane thickness determined a rise in the mass transfer resistance of CO_2 through membranes pores. Accounting for both effects, when keeping the membrane outer radius constant, the increase in the membrane thickness led to a decrease in the absorption efficiency of CO_2 (Figure 16). For the outer membrane radius of 0.3 mm, the CO_2 removal efficiency was reduced from about 91% at a membrane thickness of 0.025 mm to nearly 76.5% when the membrane thickness was increased to 0.2 mm. By increasing the outer radius of the membranes from 0.3 mm to 0.4 mm, at a constant membrane thickness of 0.1 mm, the absorption efficiency of CO_2 increased from 86% to about 94.2%, respectively. The change was primarily due to the increase in the mass transfer area between the gas and liquid, but also because of a reduction in gas velocity, thus increasing the residence time of the gas.
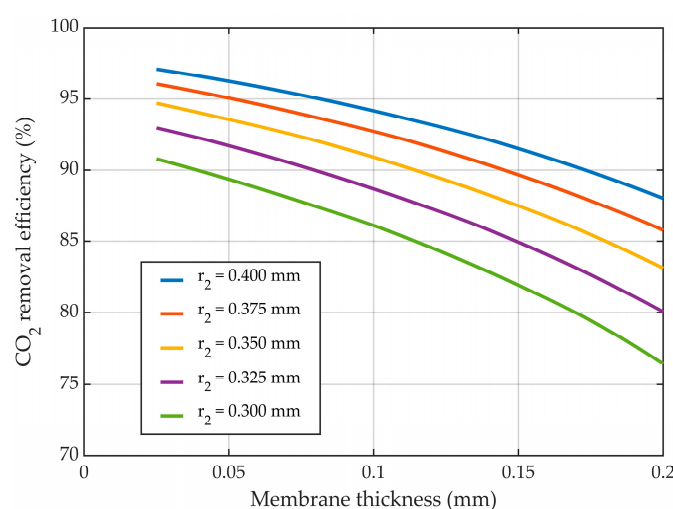

Figure 16. CO_2 removal efficiency at different membrane thicknesses, outside membrane radius constant, variable inner radius. $C_{MEA,0}$ = 818 mol/m^3 (5 wt%), $C_{CO_2,0}$ = 4.06 mol/m^3 (10 vol%), Q_g = 2 L/min, Q_L = 25 L/h.

The CO_2 gas concentration profiles in tubes and membranes at constant outer radius values are presented in Figure 17. The concentration decreased along the length of the membrane due to the absorption in the liquid phase. By increasing the membrane thickness, the mass transfer resistance of CO_2 through the membranes was increased, thus resulting in an increase in the CO_2 gradient concentration in the membranes. In addition, by reducing the inner radius of the membranes, the residence time of the gas mixture inside the tubes decreased, resulting in a higher CO_2 concentration in the exit gas and a lower absorption efficiency.

3.5.3. Variable Membrane Thickness—r_1 Constant

Maintaining the inner radius of the membrane constant, the mass transfer resistance of CO_2 through the gas phase was also kept constant. The increase in the membrane thickness led to a higher mass transfer resistance of CO_2 through the pores of the membrane, as well as an increase in the outer radius of the membranes, which determined an increase in the mass transfer area between the gas mixture and liquid solution. Considering the sum outcome of these two opposite effects on the absorption efficiency of CO_2, at lower values for the membrane thickness, the effect related to the membrane CO_2 mass transfer resistance was lower than the effect of the increase in the mass transfer area, resulting in an overall positive effect on the efficiency of absorption. By continuing to increase the membrane thickness, a maximum in CO_2 removal efficiency was observed at different values of thickness based on the inner radius of the membranes. By further increasing the

thickness, the mass transfer resistance of the membranes also increased, leading to a higher overall negative effect on the absorption efficiency.
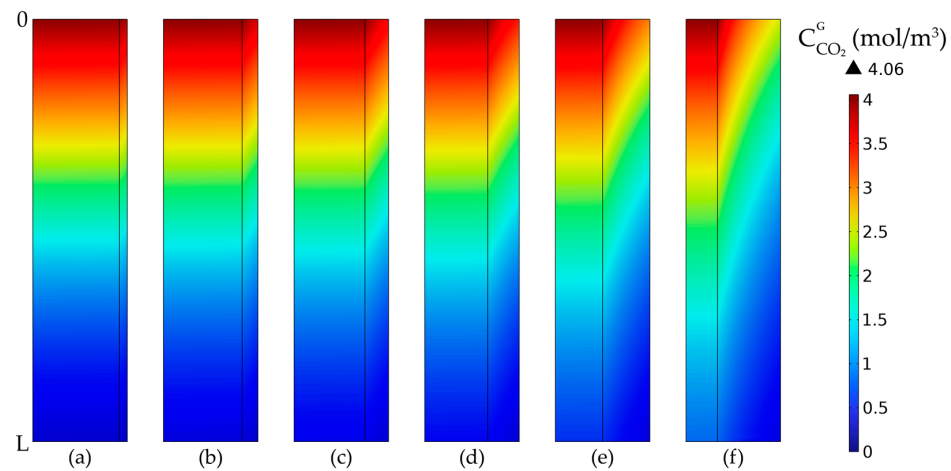

Figure 17. CO_2 gas concentration profiles in tubes and membranes at a constant outside radius of $r_2 = 0.3$ mm and different membrane thicknesses: (**a**) $\delta = 0.025$ mm, (**b**) $\delta = 0.05$ mm, (**c**) $\delta = 0.075$ mm, (**d**) $\delta = 0.1$ mm, (**e**) $\delta = 0.15$ mm, (**f**) $\delta = 0.2$ mm. $C_{MEA,0} = 818$ mol/m^3 (5 wt%), $C_{CO_2,0} = 4.06$ mol/m^3 (10 vol%), $Q_g = 2$ L/min, $Q_L = 25$ L/h.

The effect of the membrane thickness for a constant inner radius on the CO_2 removal efficiency is represented in Figure 18. At a membrane inner radius of 0.2 mm, by increasing the membrane thickness from 0.025 mm to 0.4 mm, the CO_2 removal efficiency was increased from around 81% to a maximum of about 88% at a thickness of 0.22 mm, after which the removal efficiency decreased to nearly 87%. At different values for the membrane's inner radius, the maximum values of absorption efficiency were seen at various values for membrane thickness. With increasing inner radius values, the absorption efficiency peaked at lower values for the membrane thickness. For an inner radius of 0.225 mm, the maximum value for the removal efficiency (i.e., nearly 90%) was observed at a thickness of 0.2 mm, while for the lowest inner radius of 0.15 mm, the maximum (i.e., about 83.5%) was noticed at a membrane thickness of around 0.26 mm.
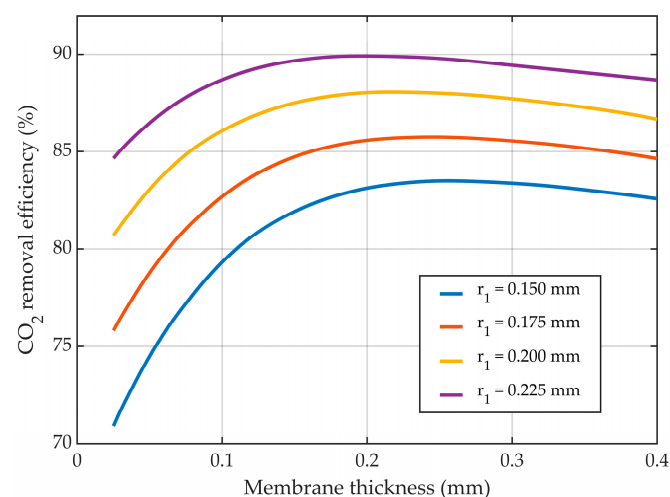

Figure 18. CO_2 removal efficiency at different membrane thicknesses, for different constant inside radii, and variable outer radii. $C_{MEA,0} = 818$ mol/m^3 (5 wt%), $C_{CO_2,0} = 4.06$ mol/m^3 (10 vol%), $Q_g = 2$ L/min, $Q_L = 25$ L/h.

The CO_2 gas concentration profiles in tubes and membranes, for constant inner radius values and different membrane thickness values, are represented in Figure 19. The CO_2

concentration in the gas phase decreased along the length and radius of the membranes due to the absorption process. By increasing the membrane thickness, the CO_2 mass transfer resistance was increased together with the concentration gradient inside the membrane.
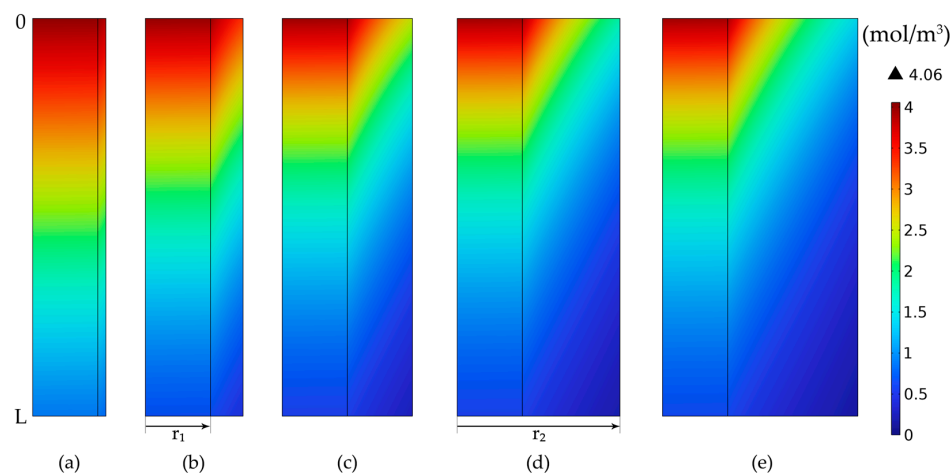

Figure 19. CO_2 gas concentration profile in tubes and membranes over the membranes' length and radius, at a constant membrane inside radius $r_1 = 0.2$ mm. (**a**) $r_2 = 0.225$ mm, (**b**) $r_2 = 0.3$ mm, (**c**) $r_2 = 0.4$ mm, (**d**) $r_2 = 0.5$ mm, (**e**) $r_2 = 0.6$ mm. $C_{MEA,0} = 818$ mol/m^3 (5 wt%), $C_{CO_2,0} = 4.06$ mol/m^3 (10 vol%), $Q_g = 2$ L/min, $Q_L = 25$ L/h.

3.6. Membrane Porosity

The membrane porosity is an important parameter in the absorption process of CO_2, with a direct impact on the efficiency of the process. The effect of the membrane porosity on the CO_2 capture rate is represented in Figure 20.
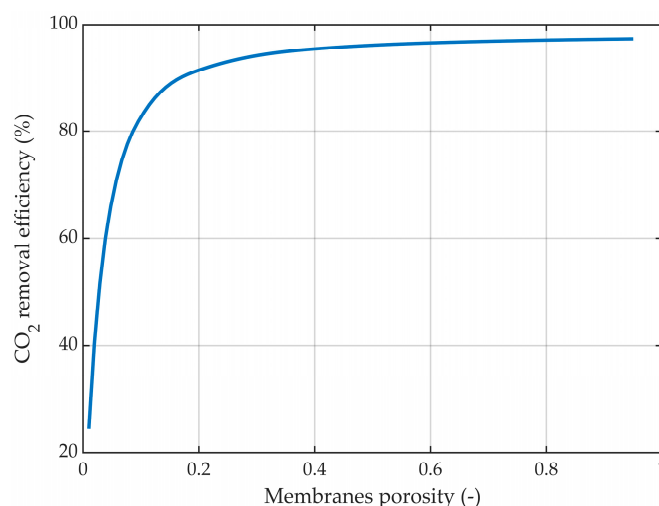

Figure 20. CO_2 removal efficiency at different membrane porosities. $r_1 = 0.225$ mm, $\delta = 0.2$ mm, $C_{MEA,0} = 818$ mol/m^3 (5 wt%), $C_{CO_2,0} = 4.06$ mol/m^3 (10 vol%), $Q_g = 2$ L/min, $Q_L = 25$ L/h.

By increasing the porosity while maintaining constant membrane dimensions, the absorption efficiency increased from about 24.5% at a porosity of 0.01 to around 97.3% at a porosity of 0.95. However, at porosity values lower than 0.2, the increase in the absorption efficiency was considerably higher. The increase from a porosity of 0.01 to 0.2 led to an increase in absorption efficiency of around 67%, while a porosity increase from 0.2 to 1 determined an increase in absorption efficiency of only around 6%.

The CO_2 concentration profiles inside the membrane tube compartments and inside the membranes, at different porosities, are represented in Figure 21, considering the same

membrane dimensions in all cases. In all cases, the CO_2 concentration in the gas phase decreased along the tubes and length and radius of the membranes due to the absorption in the aqueous MEA solution. Because of the diffusion phenomena, a concentration gradient was observed, with the gradient being more pronounced in the membranes compared to the tubes. At a lower porosity, the final concentration of CO_2 in the purified gases was higher than at a higher porosity, resulting in an improvement in the absorption efficiency with the increase in the membranes' porosity. At a porosity of 0.01, the CO_2 concentration in the gas phase at the exit reached nearly 3.07 mol/m^3 (Figure 21a), but increasing the porosity to 0.1 resulted in a decrease of the exit concentration to around 0.69 mol/m^3 (Figure 21f), and further increasing the porosity to 0.8 led to a decrease in CO_2 concentration to around 0.12 mol/m^3 (Figure 21j).
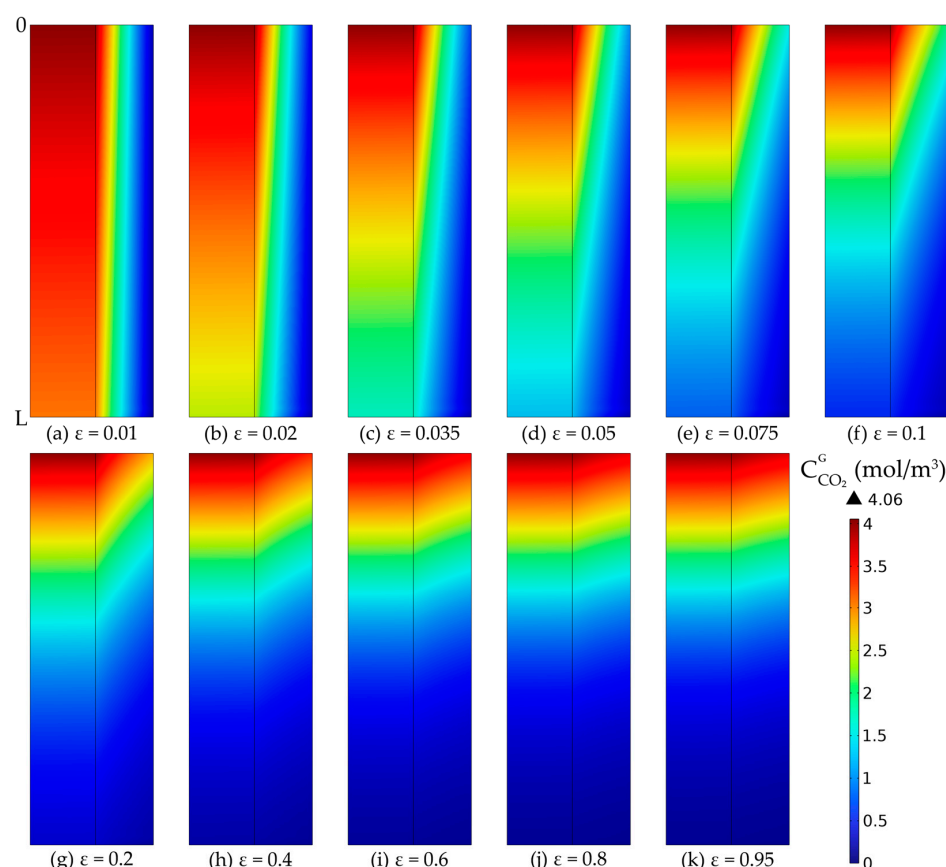

Figure 21. CO_2 gas concentration profiles in tubes and membranes wall, at a constant membrane radius (r_1 = 0.225 mm) and thickness (δ = 0.2 mm) and different porosities: (**a**) ε = 0.01, (**b**) ε = 0.02, (**c**) ε = 0.035, (**d**) ε = 0.05, (**e**) ε = 0.075, (**f**) ε = 0.1, (**g**) ε = 0.2, (**h**) ε = 0.4, (**i**) ε = 0.6, (**j**) ε = 0.8, (**k**) ε = 0.95. $C_{MEA,0}$ = 818 mol/m^3 (5 wt%), $C_{CO_2,0}$ = 4.06 mol/m^3 (10 vol%), Q_g = 2 L/min, Q_L = 25 L/h.

4. Conclusions

A 3D-CFD model of a hollow-fiber membrane contactor for the CO_2 capture process using an aqueous MEA solution was developed and implemented in COMSOL Multiphysics, considering the entire HFMC geometry. The model described the absorption process of CO_2 from the gas phase, through the pores of the membrane and into the liquid solution, followed by the chemical reaction with MEA, accounting for both convection and diffusion mechanisms. The model was validated by comparing experimental data published in literature with model predictions on CO_2 capture rates at different gas and liquid flow rates, as well as different initial concentrations of the flue gases. The simulation results demonstrated excellent correlation with the experimental data, with an R^2 coefficient value exceeding 0.922. The highest CO_2 absorption efficiency was achieved at a high liquid flow rate, low gas flow rate, and low CO_2 concentration in the inflow gas.

Additionally, the optimal mode for fluid flow inside the HFMC was studied, considering identical operating conditions and a counter-current arrangement. The simulation results indicated that superior CO_2 capture rates were achieved when the gas mixture flowed inside the membranes and the liquid absorption solution ran between them. Furthermore, the effect of the membrane dimensions (i.e., radius and thickness) on the capture process of CO_2 using HFMC was investigated. Increasing the membrane radius, while maintaining a constant thickness, positively influenced the efficiency of the process due to the higher mass transfer area and longer residence time of the gas phase. On the other hand, higher membrane thickness resulted in higher CO_2 mass transfer resistance. In order to maximize the absorption efficiency, the findings indicate a low membrane thickness, with optimal dimensions being an inner radius of 0.225 mm and a membrane thickness of 0.2 mm. Additionally, the effect of porosity on the absorption process was investigated, revealing that increasing the porosity led to an improved CO_2 capture efficiency, but with significant impact only for porosity values below 0.2 and a lesser influence for porosities above that threshold.

Author Contributions: Conceptualization, A.-C.B. and V.-C.S.; methodology, V.-C.S. and A.-M.C.; software, V.-C.S.; validation, A.-C.B., V.-C.S. and A.-M.C.; formal analysis, A.-C.B.; investigation, A.-C.B. and V.-C.S.; resources, C.-C.C.; data curation, V.-C.S., C.-C.C. and A.-M.C.; writing—original draft preparation, A.-C.B.; writing—review and editing, C.-C.C. and A.-M.C.; visualization, V.-C.S. and A.-M.C.; supervision, C.-C.C. and A.-M.C.; project administration, C.-C.C. and A.-M.C.; funding acquisition, C.-C.C. All authors have read and agreed to the published version of the manuscript.

Institutional Review Board Statement: Not applicable.

Data Availability Statement: The original contributions presented in the study are included in the article. Further inquiries can be directed to the corresponding author.

Conflicts of Interest: The authors declare no conflicts of interest.

Nomenclature

c	concentration of species (mol/m^3)
d_1	membrane inside diameter (m)
d_h	hydraulic diameter (m)
d_{lm}	logarithmic diameter (m)
$D_{j,i}, D_{j,mem}$	diffusion coefficient of species j in phase i and membrane (m^2/s)
E	enhancement factor (-)
H_{CO_2}	Henry's coefficient of CO_2 in the liquid MEA solution (-)
J_{CO_2}	CO_2 mass transfer flux from gas to liquid $(mol/m^2 \ s)$
$k_{CO_2,i}, k_{CO_2,mem}$	partial CO_2 mass transfer coefficient in the i phase and through membrane pores (m/s)
K_L	global CO_2 mass transfer coefficient (m/s)
L	membranes length (m)
n	number of membranes (-)
P	pressure (bar)
Q	volumetric flow rate (m^3/s)
r_1	membrane inside radius (m)
r_2	membrane outside radius (m)
r_{mod}	module inner radius (m)
r_p	average membranes pores radius (m)
R_{CO_2}	reaction rate $(mol/m^3 \ s)$
Re	Reynolds number (-)
Sc	Schmidt number (-)
Sh	Sherwood number (-)
T	temperature (K)
u	superficial fluid velocity (m/s)

Superscripts/subscripts	
i	gas (g) and liquid (L) phase
j	system components
Greek letters	
δ_{mem}	membrane thickness (m)
ε_{mem}	membrane porosity (-)
μ	dynamic viscosity (Pa s)
ρ	fluid density (kg/m^3)
τ_{mem}	membrane tortuosity (-)

References

1. Nocito, F.; Dibenedetto, A. Atmospheric CO_2 Mitigation Technologies: Carbon Capture Utilization and Storage. *Curr. Opin. Green Sustain. Chem.* **2020**, *21*, 34–43. [CrossRef]
2. Eskandari, M.; Khaksar, S.A.N.; Keshavarz, P. CO_2 Absorption Using Benzylamine as Absorbent and Promoter in a Hollow Fiber Membrane Contactor: A Numerical Study. *J. CO2 Util.* **2022**, *66*, 102287. [CrossRef]
3. Storrs, K.; Lyhne, I.; Drustrup, R. A Comprehensive Framework for Feasibility of CCUS Deployment: A Meta-Review of Literature on Factors Impacting CCUS Deployment. *Int. J. Greenh. Gas Control* **2023**, *125*, 103878. [CrossRef]
4. Gkotsis, P.; Peleka, E.; Zouboulis, A. Membrane-Based Technologies for Post-Combustion CO_2 Capture from Flue Gases: Recent Progress in Commonly Employed Membrane Materials. *Membranes* **2023**, *13*, 898. [CrossRef]
5. Wang, Z.; Liu, L.; Ren, T.; Gao, P.; Sang, H.; Yang, X.; Li, Z.; Wang, Z.; Li, S.; Li, G.K. Carbon Capture from Humid Gases Using Alkaline-Promoted Polypyrrole by a Vacuum Swing Adsorption Process. *Sep. Purif. Technol.* **2023**, *323*, 124399. [CrossRef]
6. Entesari, N.; Divsalar, A.; Tsotsis, T.T. Modeling and Simulation of a Reactive Separation System for Carbon Capture and Utilization in Biogas Streams. *Chem. Eng. Process.-Process Intensif.* **2020**, *156*, 108093. [CrossRef]
7. Vadillo, J.M.; Díaz-Sainz, G.; Gómez-Coma, L.; Garea, A.; Irabien, A. Chemical and Physical Ionic Liquids in CO_2 Capture System Using Membrane Vacuum Regeneration. *Membranes* **2022**, *12*, 785. [CrossRef]
8. Fu, L.; Ren, Z.; Si, W.; Ma, Q.; Huang, W.; Liao, K.; Huang, Z.; Wang, Y.; Li, J.; Xu, P. Research Progress on CO_2 Capture and Utilization Technology. *J. CO2 Util.* **2022**, *66*, 102260. [CrossRef]
9. Ding, H.; Zhang, Y.; Dong, Y.; Wen, C.; Yang, Y. High-Pressure Supersonic Carbon Dioxide (CO_2) Separation Benefiting Carbon Capture, Utilisation and Storage (CCUS) Technology. *Appl. Energy* **2023**, *339*, 120975. [CrossRef]
10. Gabelman, A.; Hwang, S.-T. Hollow Fiber Membrane Contactors. *J. Membr. Sci.* **1999**, *159*, 61–106. [CrossRef]
11. Mansourizadeh, A.; Ismail, A.F. Hollow Fiber Gas–Liquid Membrane Contactors for Acid Gas Capture: A Review. *J. Hazard. Mater.* **2009**, *171*, 38–53. [CrossRef]
12. Xia, J.; Zhang, Z.; Wang, L.; Wang, F.; Miao, H.; Zhang, H.; Xia, L.; Yuan, J. Performance Evaluation and Optimization of Hollow Fiber Membrane Contactors for Carbon Dioxide Absorption: A Comparative Study of Ammonia, Ethanolamine, and Diethanolamine Solvents. *J. Environ. Chem. Eng.* **2023**, *11*, 111354. [CrossRef]
13. Cesari, L.; Castel, C.; Favre, E. Membrane Contactors for Intensified Gas-Liquid Absorption Processes with Physical Solvents: A Critical Parametric Study. *J. Membr. Sci.* **2021**, *635*, 119377. [CrossRef]
14. Taghvaie Nakhjiri, A.; Heydarinasab, A.; Bakhtiari, O.; Mohammadi, T. Numerical Simulation of CO_2/H_2S Simultaneous Removal from Natural Gas Using Potassium Carbonate Aqueous Solution in Hollow Fiber Membrane Contactor. *J. Environ. Chem. Eng.* **2020**, *8*, 104130. [CrossRef]
15. Rivero, J.R.; Panagakos, G.; Lieber, A.; Hornbostel, K. Hollow Fiber Membrane Contactors for Post-Combustion Carbon Capture: A Review of Modeling Approaches. *Membranes* **2020**, *10*, 382. [CrossRef]
16. Mavroudi, M.; Kaldis, S.P.; Sakellaropoulos, G.P. A Study of Mass Transfer Resistance in Membrane Gas–Liquid Contacting Processes. *J. Membr. Sci.* **2006**, *272*, 103–115. [CrossRef]
17. Kumar, P.S.; Hogendoorn, J.A.; Feron, P.H.M.; Versteeg, G.F. Approximate Solution to Predict the Enhancement Factor for the Reactive Absorption of a Gas in a Liquid Flowing through a Microporous Membrane Hollow Fiber. *J. Membr. Sci.* **2003**, *213*, 231–245. [CrossRef]
18. Rode, S.; Nguyen, P.T.; Roizard, D.; Bounaceur, R.; Castel, C.; Favre, E. Evaluating the Intensification Potential of Membrane Contactors for Gas Absorption in a Chemical Solvent: A Generic One-Dimensional Methodology and Its Application to CO_2 Absorption in Monoethanolamine. *J. Membr. Sci.* **2012**, *389*, 1–16. [CrossRef]
19. Saeed, M.; Deng, L. Post-Combustion CO_2 Membrane Absorption Promoted by Mimic Enzyme. *J. Membr. Sci.* **2016**, *499*, 36–46. [CrossRef]
20. Khaisri, S.; deMontigny, D.; Tontiwachwuthikul, P.; Jiraratananon, R. A Mathematical Model for Gas Absorption Membrane Contactors That Studies the Effect of Partially Wetted Membranes. *J. Membr. Sci.* **2010**, *347*, 228–239. [CrossRef]
21. Chu, Y.; Lindbråthen, A.; Lei, L.; He, X.; Hillestad, M. Mathematical Modeling and Process Parametric Study of CO_2 Removal from Natural Gas by Hollow Fiber Membranes. *Chem. Eng. Res. Des.* **2019**, *148*, 45–55. [CrossRef]

22. Boributh, S.; Rongwong, W.; Assabumrungrat, S.; Laosiripojana, N.; Jiraratananon, R. Mathematical Modeling and Cascade Design of Hollow Fiber Membrane Contactor for CO_2 Absorption by Monoethanolamine. *J. Membr. Sci.* **2012**, *401–402*, 175–189. [CrossRef]

23. Bozonc, A.-C.; Cormos, A.-M.; Dragan, S.; Dinca, C.; Cormos, C.-C. Dynamic Modeling of CO_2 Absorption Process Using Hollow-Fiber Membrane Contactor in MEA Solution. *Energies* **2022**, *15*, 7241. [CrossRef]

24. Al-Marzouqi, M.H.; El-Naas, M.H.; Marzouk, S.A.M.; Al-Zarooni, M.A.; Abdullatif, N.; Faiz, R. Modeling of CO_2 Absorption in Membrane Contactors. *Sep. Purif. Technol.* **2008**, *59*, 286–293. [CrossRef]

25. Hosseinzadeh, A.; Hosseinzadeh, M.; Vatani, A.; Mohammadi, T. Mathematical Modeling for the Simultaneous Absorption of CO_2 and SO_2 Using MEA in Hollow Fiber Membrane Contactors. *Chem. Eng. Process. Process Intensif.* **2017**, *111*, 35–45. [CrossRef]

26. Shirazian, S.; Pishnamazi, M.; Rezakazemi, M.; Nouri, A.; Jafari, M.; Noroozi, S.; Marjani, A. Implementation of the Finite Element Method for Simulation of Mass Transfer in Membrane Contactors. *Chem. Eng. Technol.* **2012**, *35*, 1077–1084. [CrossRef]

27. Faiz, R.; Al-Marzouqi, M. CO_2 Removal from Natural Gas at High Pressure Using Membrane Contactors: Model Validation and Membrane Parametric Studies. *J. Membr. Sci.* **2010**, *365*, 232–241. [CrossRef]

28. Goyal, N.; Suman, S.; Gupta, S.K. Mathematical Modeling of CO_2 Separation from Gaseous-Mixture Using a Hollow-Fiber Membrane Module: Physical Mechanism and Influence of Partial-Wetting. *J. Membr. Sci.* **2015**, *474*, 64–82. [CrossRef]

29. Rezakazemi, M.; Niazi, Z.; Mirfendereski, M.; Shirazian, S.; Mohammadi, T.; Pak, A. CFD Simulation of Natural Gas Sweetening in a Gas–Liquid Hollow-Fiber Membrane Contactor. *Chem. Eng. J.* **2011**, *168*, 1217–1226. [CrossRef]

30. Shirazian, S.; Moghadassi, A.; Moradi, S. Numerical Simulation of Mass Transfer in Gas–Liquid Hollow Fiber Membrane Contactors for Laminar Flow Conditions. *Simul. Model. Pract. Theory* **2009**, *17*, 708–718. [CrossRef]

31. Nakhjiri, A.T.; Heydarinasab, A.; Bakhtiari, O.; Mohammadi, T. Experimental Investigation and Mathematical Modeling of CO_2 Sequestration from CO_2/CH_4 Gaseous Mixture Using MEA and TEA Aqueous Absorbents through Polypropylene Hollow Fiber Membrane Contactor. *J. Membr. Sci.* **2018**, *565*, 1–13. [CrossRef]

32. Vadillo, J.M.; Gómez-Coma, L.; Garea, A.; Irabien, A. CO_2 Desorption Performance from Imidazolium Ionic Liquids by Membrane Vacuum Regeneration Technology. *Membranes* **2020**, *10*, 234. [CrossRef] [PubMed]

33. Pozzobon, V.; Perré, P. Mass Transfer in Hollow Fiber Membrane Contactor: Computational Fluid Dynamics Determination of the Shell Side Resistance. *Sep. Purif. Technol.* **2020**, *241*, 116674. [CrossRef]

34. Cai, J.J.; Hawboldt, K.; Abdi, M.A. Analysis of the Effect of Module Design on Gas Absorption in Cross Flow Hollow Membrane Contactors via Computational Fluid Dynamics (CFD) Analysis. *J. Membr. Sci.* **2016**, *520*, 415–424. [CrossRef]

35. Boucif, N.; Corriou, J.P.; Roizard, D.; Favre, E. Carbon Dioxide Absorption by Monoethanolamine in Hollow Fiber Membrane Contactors: A Parametric Investigation. *AIChE J.* **2012**, *58*, 2843–2855. [CrossRef]

36. Yang, M.-C.; Cussler, E.L. Designing Hollow-Fiber Contactors. *AIChE J.* **1986**, *32*, 1910–1916. [CrossRef]

37. Ghobadi, J.; Ramirez, D.; Jerman, R.; Crane, M.; Khoramfar, S. CO_2 Separation Performance of Different Diameter Polytetrafluoroethylene Hollow Fiber Membranes Using Gas-Liquid Membrane Contacting System. *J. Membr. Sci.* **2018**, *549*, 75–83. [CrossRef]